ACS APPLIED MATERIALS & INTERFACES

Research Article

www.acsami.org

One- and Three-Dimensional Growth of Hydroxyapatite Nanowires during Sol–Gel–Hydrothermal Synthesis

Daniel O. Costa,[†] S. Jeffrey Dixon,[‡,§] and Amin S. Rizkalla[†,§,*]

[†]Department of Chemical and Biochemical Engineering, Faculty of Engineering, The University of Western Ontario, London, Ontario, Canada N6A 5B9

[‡]Department of Physiology and Pharmacology, Schulich School of Medicine & Dentistry, The University of Western Ontario, London, Ontario, Canada N6A 5C1

[§]Schulich Dentistry, Schulich School of Medicine & Dentistry, The University of Western Ontario, London, Ontario, Canada N6A 5C1

Supporting Information

ABSTRACT: Nanoscale hydroxyapatite (HA) is an optimal candidate biomaterial for bone tissue engineering because of its bioactive and osteoconductive properties. In this study, micro- and nanoscale HA particles with rod- and wirelike morphology were synthesized by a novel sol–gel–hydrothermal process. Sol–gel chemistry was used to produce a dry gel containing amorphous calcium phosphate (ACP), which was used as a precursor material in a hydrothermal process. The sol–gel–hydrothermal products were characterized by scanning electron microscopy (SEM), X-ray diffraction (XRD), and Fourier transform infrared spectroscopy (FTIR) to determine particle morphology, crystal structure, and the presence of chemical functional groups. A pure HA crystal was synthesized, which underwent both one- and three-dimensional growth, resulting in tunable microrod and nanorod, and wire morphologies. The effects of solution pH and reaction time on particle diameter and length were assessed. Particle diameter ranged from 25 to 800 nm and decreased with an increase in solution pH, whereas both particle length and diameter increased as the hydrothermal process was prolonged. Nanowire HA powders (10–50 wt %) were mixed with poly(ε-caprolactone) (PCL) to produce PCL/HA composites. Fracture surfaces of PCL/HA composites showed a well-dispersed and homogeneous distribution of HA nanowires within the PCL matrix. Mechanical testing revealed a significant ($p < 0.05$) increase in the Young's and compressive moduli of PCL/HA composites compared to PCL alone, with 50 wt % HA producing a 3-fold increase in Young's modulus from 193 to 665 MPa and 2-fold increase in compressive modulus from 230 to 487 MPa. These HA nanowires can be used to reinforce polymer composites and are excellent biomaterials for tissue engineering of bone.

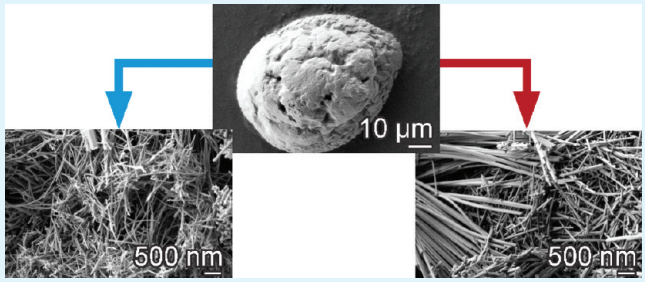

KEYWORDS: *hydrothermal, hydroxyapatite, nanorods, nanowires, polycaprolactone, sol–gel*

1. INTRODUCTION

Hydroxyapatite (HA), $Ca_{10}(PO_4)_6(OH)_2$, is a synthetic ceramic that has attracted much attention for biomedical applications because of its chemical and structural similarity to the mineral constituent of human bone and teeth.[1] HA is biocompatible and osteoconductive,[2] serving as an excellent biomaterial for use as bone graft substitutes[3] and implant coatings.[4] In particular, HA powders consisting of micro- and nanosized particles can be used to reinforce polymer composites[5,6] and calcium-phosphate bone cements.[7,8]

Two common methods of HA synthesis are sol–gel and hydrothermal processes. Sol–gel synthesis methods involve atomic level molecular mixing, providing control of composition and chemical homogeneity.[9,10] However, sol–gel powders require calcination at high temperature in the presence of air to produce crystalline products. Moreover, sol–gel HA synthesis is often accompanied by the formation of secondary phases such as calcium oxide and tricalcium phosphate (TCP),[9,10] and gives rise to granular particle shapes.[10,11] Alternatively, HA powders with controlled particle size, morphology, and crystallinity have been successfully synthesized by a variety of hydrothermal methods.[12,13] Hydrothermal homogeneous precipitation is capable of producing HA whiskers with high aspect ratio.[14] However, the HA whiskers have diameter and length scales in the micrometer-range, and it is known that having at least one dimension in the nanoscale size range optimizes the biological and mechanical functionality of HA.[15–17] Recently, HA nanowires and hollow microspheres were synthesized by hydrothermal processing of xonolite nanowire and calcium carbonate microsphere precursors of similar micro- and

Received: December 7, 2011
Accepted: February 1, 2012
Published: February 1, 2012

nanoscale dimensions.[18] It was found that the scale and structure of the precursor material dictated the final morphologies of the HA product. Furthermore, hydrothermal treatment of calcium silicate-based starting materials can produce various element-substituted HA nanostructures.[19] Thus, in hydrothermal processes, characteristics of the precursors determine crystal nucleation and growth, and therefore dictate the final morphology of the product.

Surfactants and reverse micelle solutions in solvothermal processes can be used to produce nanowires and nanorods of varying aspect ratios.[20−22] Surfactants provide organized organic templates that guide the synthesis and growth of inorganic nanomaterials through geometric, electrostatic and stereochemical interactions. However, HA products from solvothermal synthesis are typically of low aspect ratio,[21−23] and highly aggregated,[20,23] and the presence of surfactants and solvents during the solvothermal process may result in undesired organic components being incorporated into the final HA products.[21,23,24] Therefore, the goal of the present study was to develop a method for the synthesis of HA nanowires with high aspect ratio.

In the present study, a novel method is presented for the synthesis of HA nanowires with high aspect ratio. Sol−gel chemistry was used to produce a nanoscale amorphous calcium phosphate (ACP). The subsequent nano-ACP was subjected to hydrothermal treatment in aqueous solvent to induce the formation of crystalline HA micro- and nanowires. To the best of our knowledge, this is the first report of the synthesis of high-purity HA nanowires by a tunable crystal growth mechanism using a combination sol−gel−hydrothermal method. By varying the initial pH of the aqueous solvent/sol−gel precursor mixture and the hydrothermal synthesis time, we obtained HA powders with varying particle diameters and lengths. This aqueous based hydrothermal treatment of a sol−gel product is a simple, cost-effective, and environmentally friendly synthesis route, offering a high degree of control on the particle morphology of the HA product. The as produced nanoscale HA powders were used as a reinforcing filler in polycaprolactone (PCL) composites. These nanoscale HA-embedded PCL composites mimic the nanoapatite/collagen composite of bone. Therefore, such materials are excellent candidates for the production of scaffolds for bone tissue engineering applications.

2. MATERIALS AND METHODS

Materials. Triethyl phosphite (TEP, 98%), calcium nitrate tetrahydrate ($CaNO_3{\cdot}4H_2O$, 99%), sodium hydroxide (NaOH, 98.5%), ammonium hydroxide (NH_4OH, 30%), anhydrous ethanol (EtOH), and dichloromethane (DCM, 99.5%) were purchased from Sigma-Aldrich (Milwaukee, WI). Poly(ε-caprolactone) (PCL) (CAPA 6800, MW 80 000 g/mol) was generously donated by Solvay Chemicals Inc. (Houston, TX).

Preparation of Dried Calcium Phosphate (CaP) Gel. A dry CaP gel was prepared by a sol−gel method similar to that developed by Liu et al.[10] Briefly, TEP solution was diluted in EtOH such that the concentration was 1.8 M. A small amount of water was added to the phosphite sol (6:1 molar ratio), and the mixture was sealed in a round-bottom flask and stirred vigorously for 30 min. The solution was allowed to age for 24 h to ensure complete hydrolysis of phosphite. A stoichiometric amount of $CaNO_3{\cdot}4H_2O$ dissolved in EtOH, was added dropwise to the phosphite sol such that the Ca/P = 1.67. The resulting mixture was stirred vigorously for 30 min and aged at room temperature for 24 h. The sol was dried at 80 °C to produce a white gel, which was ground to a fine powder using a mortar and pestle.

Hydrothermal Treatment. For hydrothermal treatment, 0.5 g of the dried CaP gel was suspended in 30 mL aqueous solution and vigorously stirred for 30 min. Aqueous solutions used as suspension medium were selected to achieve the desired pH. Aqueous solvents included deionized H_2O, NH_4OH (0.1 M) and NaOH (5 M). Suspensions were ultrasonically treated for 5 min and vigorously stirred for 30 min. The effect of pH on HA synthesis and particle morphology was determined by setting the initial pH of the CaP gel aqueous suspension to 5.20, 7.50, or 13.70. Suspensions were poured into a 125 mL Teflon-lined acid digestion bomb (Parr Instrumentation Company, Moline, IL) and heated to 170 °C using a band heater. Heating was regulated using a thermocouple, and a temperature and process controller (iSeries, Omega, Stamford, CT). For each initial pH condition, the hydrothermal treatment time was 6, 16, or 24 h. At the end of each time period, the bomb was cooled by means of a fan to room temperature and the product, which formed as white precipitates, had settled to the bottom of the Teflon liner. The aqueous solvent was carefully decanted and the particles were collected, washed with deionized H_2O several times, and sedimented. The recovered pellet was dried at 50 °C and ground into a fine powder using a mortar and pestle.

Scanning Electron Microscopy (SEM) and Energy-Dispersive X-ray Spectroscopy (EDX). Particle morphology was examined using a FIB/SEM LEO 1540XB microscope (Carl Zeiss, Göttingen, Germany) equipped with an energy-dispersive X-ray spectrometer for elemental analysis. Samples were first coated with 3 nm osmium metal using a Filgen OPC-80T instrument. Representative images were selected from three fields of view for each synthesis condition. Mean particle diameter calculations were determined by measuring a total of 300 particles from three fields of view (n = 300) using ImageJ software (National Institutes of Health, USA). Elemental analysis of powders was performed by EDX on three fields of view for each synthesis condition (n = 3).

X-ray Diffraction Analysis (XRD). Crystal structures of the powders were determined by XRD using a Rotaflex RTP 300 RC (Rigaku Co., Japan) operating on CoKα radiation at 45 kV and 160 mA. Spectra were collected in the 2θ range between 5 and 65°, with 0.05° step and 10°/min scan speed. 2θ for equivalent CuKα radiation was obtained using Bragg's Law, $\lambda = 2d\sin\theta$, where λ = 1.54056 and 1.79026 Å for Cu and Co, respectively.[25]

Fourier Transform Infrared Spectroscopy (FTIR). Functional group identification of the CaP gel and hydrothermally synthesized powders were obtained by FTIR using a Bruker Vector 22 (Bruker Optics LTD, Milton, ON). Specimens were prepared by mixing 4 wt % of each sample with potassium bromide (KBr) and then pressing into a pellet. Specimens were analyzed at a resolution of 4 cm^{-1} and transmittance spectra from 4000 to 500 cm^{-1} wavenumbers were collected.

Preparation of PCL and PCL/HA Composites. PCL specimens were prepared by dissolving PCL pellets in DCM to produce a 12 wt % PCL mixture. The solvent was allowed to evaporate in a fume hood to yield a PCL film. The PCL film was heat-pressed at 100 °C and 670 N for 2 min. PCL/HA composites were produced by adding HA powder, synthesized at a pH of 13.70 for 24 h, to DCM and then stirring for 15 min, and sonicated for 5 min. PCL was then added to the HA/DCM suspension to produce a PCL/HA slurry containing 10−50 wt % HA. The PCL/HA slurry was cast in a glass dish and the solvent evaporated in a fume hood. The resulting PCL/HA films were heat pressed at 100 °C and 670 N for 2 min. Fracture surfaces of PCL/HA composites were prepared for SEM analysis and EDX elemental mapping by submerging 60:40 (w/w) PCL:HA samples in liquid nitrogen and subsequent fracturing.

Mechanical Testing of PCL/HA Composites. Mechanical properties were determined using an Instron 3345 universal testing machine (Instron, Canton, MA) equipped with a 500 N (tension) and 5 kN (compression) load cell. For tensile testing, 10 mm × 30 mm specimens were cut from the PCL and PCL/HA films using a sharp blade. For compressive tests, cylindrical specimens (diameter = 6 mm, length = 5−9 mm) were prepared by slicing the PCL and PCL/HA films and adding 0.3 g to a stainless steel mold. The mold was heated

at 100 °C for 30 min and heat pressed at 100 °C and 670 N for 2 min. Prepared specimens were soaked in deionized H_2O at 37 °C for 24 h prior to testing. For each group, 5 independent specimens (n = 5) were tested in tension and compression at a crosshead speed of 1 mm/min. Stress−strain relationships were obtained from the load and displacement data. The Young's and compressive moduli were determined by calculating the slope of the linear portion of the stress−strain curves. The tensile strength, defined as the maximum stress achieved, and the compressive stress at 10% strain were obtained from the stress−strain curves of each specimen. Nonlinear regression analysis was performed to determine the correlation between HA content and the stiffness and strength of the PCL/HA composites.

3. RESULTS

FTIR, XRD, and SEM Analysis of CaP Gel. Drying of the aged sol at 70 °C removed the EtOH solvent and produced a white gel. FTIR (Figure 1a) and XRD (Figure 1b) spectra of the CaP gel were obtained. From FTIR of the CaP gel (Figure 1a), typical peaks attributed to PO_4^{3-} groups are seen by the sharp ν_3 P−O asymmetric stretching band at 1040 cm^{-1} and a broad band in the range of 600−500 cm^{-1}, characteristic of O−P−O bending of the ν_4 PO_4^{3-} groups in apatite.[26] This featureless broadband suggests a disordered phosphate structure in the CaP gel, indicating the presence of ACP in the CaP gel precursor.[1] Crystalline nitrate peaks are also evident at 730, 812, 1350, and 1420 cm^{-1}. P−H and P═O at 2450 and 1100 cm^{-1}, respectively, are characteristic of hydrolyzed phosphite. H_2O in the precursor produced a significant broad band at 3400 cm^{-1} and sharp peak at 1630 cm^{-1}. XRD spectra of the CaP gel (Figure 1b) confirms the presence of a crystalline nitrate in the form of $Ca(NO_3)_2$ anhydride. All visible peaks in the XRD spectra could be ascribed to $Ca(NO_3)_2$, with the major peaks at 2θ = 20.2, 26.2, and 41.1° (JCPDS 7−204).[27] SEM was performed on a large particle of the CaP gel after being ground by mortar and pestle (Figure 1c). The surfaces of CaP gel particles were featureless, typical of amorphous products.[28]

In summary, FTIR and SEM analyses of the CaP gel indicated the successful synthesis of an ACP precursor.

SEM Analysis of Powders Produced by Hydrothermal Treatment. The combination of a sol−gel method with hydrothermal treatment produced powders consisting of particles having micro- and nanowire shapes. When the initial pH of the aqueous solvent/CaP gel suspension was slightly acidic at 5.20, powders consisting of particles with diameters ranging from 20 to 800 nm were produced (Figure 2a−c). The image and frequency distribution plot at 6 h (Figure 2a) revealed short nanorods with diameters of 30 nm as determined from the best fit value of the nonlinear regression curve. Increasing the hydrothermal reaction time to 16 h (Figure 2b) resulted in growth of the long axis of the particle, with only a minor increase in the diameter. Further crystal growth was seen by extending the reaction time to 24 h, which increased particle length and radial growth (Figure 2c). The SEM images and corresponding frequency distribution plots highlight the dependence of particle morphology on hydrothermal time. Allowing the hydrothermal reaction to proceed to 24 h resulted in a large shift of the mean particle diameter to 300 nm and broadening of the particle diameter distribution plots (Figure 2d), indicating greater inhomogeneity in particle diameter. The particles varied from short nanorods with L/D (length/diameter) of ~9 at 6 h to nanowires and microwires with L/D in the range of 50−80 at both 16 and 24 h.

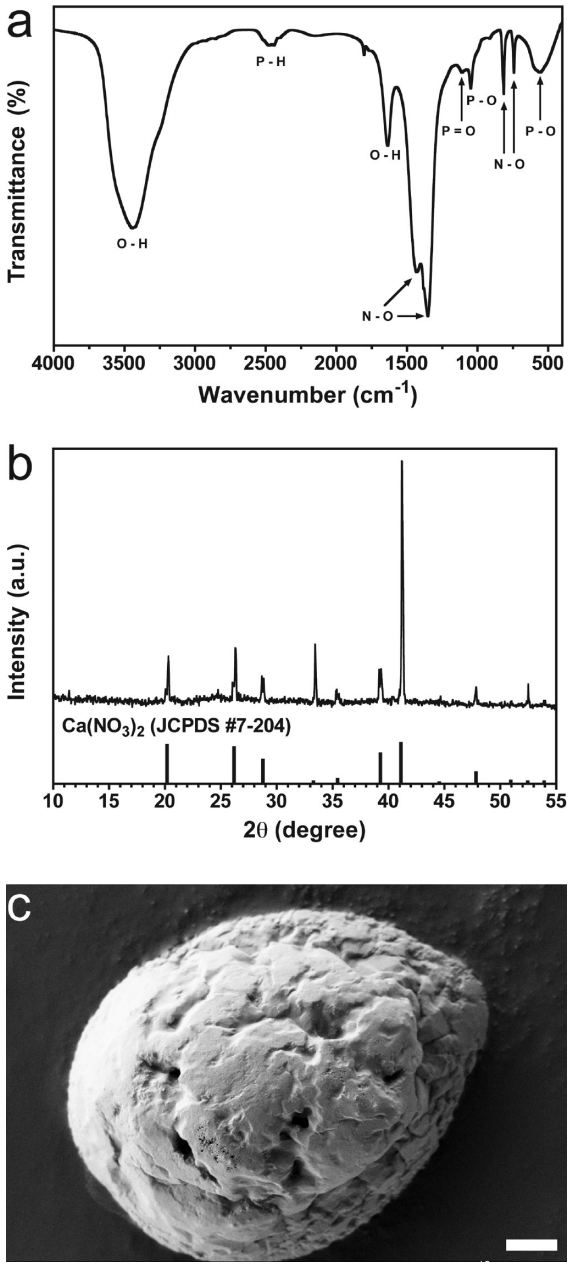

Figure 1. Dried CaP gel. (a) FTIR, (b) XRD, and (c) SEM of the CaP gel produced after drying the 24 h aged sol−gel at 70 °C. Representative of two independent samples. At the bottom of the XRD spectrum is the Joint Committee on Powder Diffraction Standards (JCPDS 7−204) pattern for $Ca(NO_3)_2$.[27] Scale bar = 1 μm.

Increasing the initial pH using NH_4OH or NaOH permitted tuning of nanowire diameter. The addition of aqueous NH_4OH (0.1 M) to H_2O slurries was used to achieve a pH of 7.50. SEM micrographs (Figure 3a−c) showed substantial reduction in particle diameter compared to powders produced under acidic conditions, with particle diameters ranging from 20 to 200 nm. Six-h hydrothermal reaction produced short nanorods having diameters of 35 nm and a narrow size distribution (Figure 3a). Extending the hydrothermal time to 16 h resulted in the formation of nanowires with growth in the long axis (Figure $3b_i$), whereas little growth was seen in the radial direction as illustrated by the comparable distribution plots at 6 and 16 h (Figure $3a_{ii}$ versus Figure $3b_{ii}$). In contrast, crystal

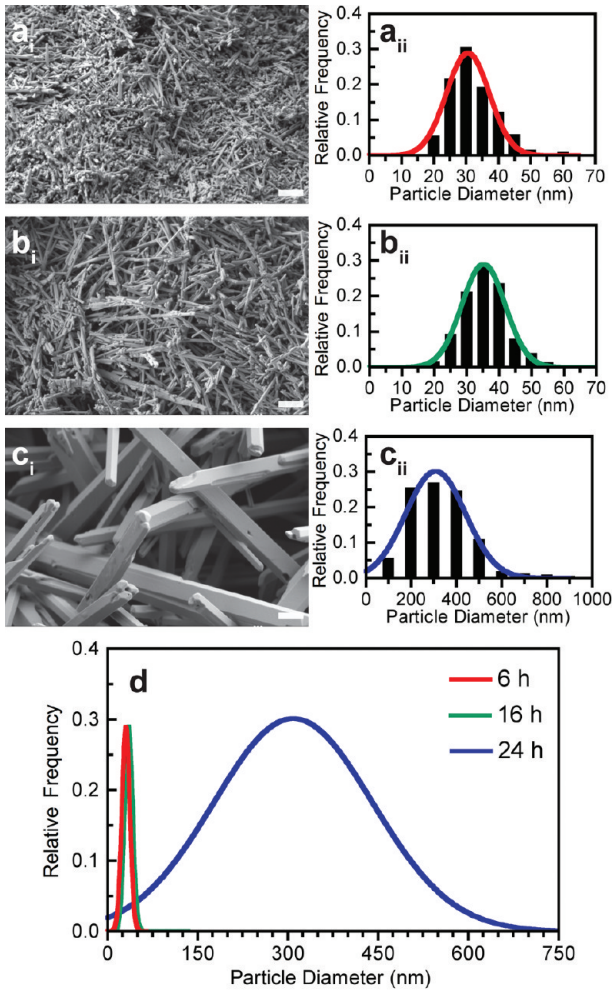

Figure 2. Hydrothermal synthesis at pH 5.20: (i) SEM images and (ii) particle diameter frequency distribution plots of CaP gel powders after hydrothermal treatment for (a) 6, (b) 16, and (c) 24 h. Hydrothermal time effect illustrated by (d) nonlinear regression curves of the particle diameter distributions obtained from measuring 100 particle diameters for three fields of view (n = 300). Scale bar = 500 nm.

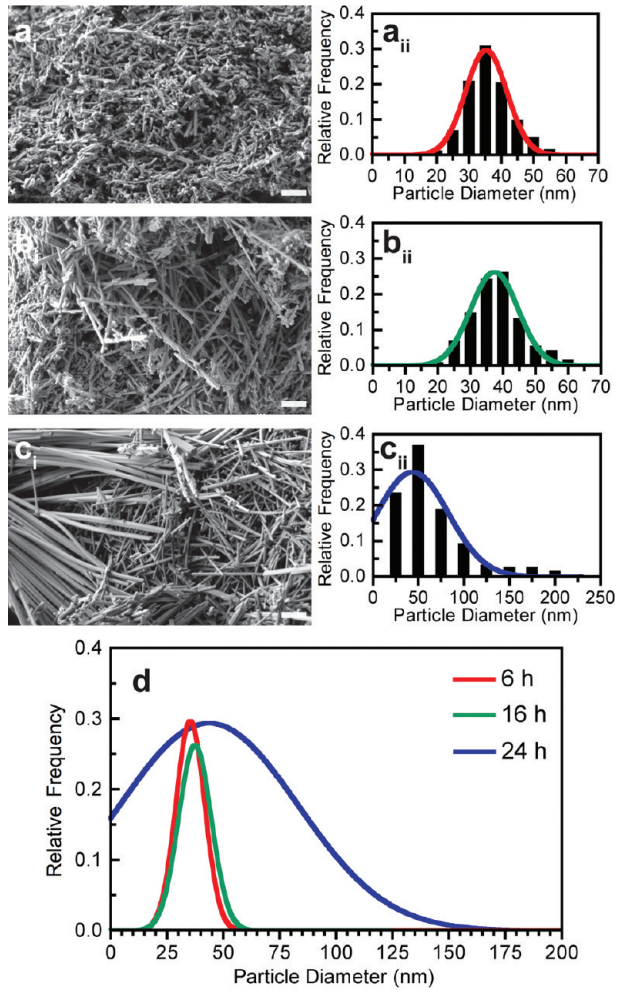

Figure 3. Hydrothermal synthesis at pH 7.50: (i) SEM images and (ii) particle diameter frequency distribution plots of CaP gel powders after hydrothermal treatment for (a) 6, (b) 16, and (c) 24 h. Hydrothermal time effect illustrated by (d) nonlinear regression curves of the particle diameter distributions obtained from measuring 100 particle diameters for three fields of view (n = 300). Scale bar = 500 nm.

growth in both the long axis and radial directions occurred at 24 h (Figure 3c), giving rise to a broad distribution in particle diameter (Figure 3c$_{ii}$). When compared to the particle morphology observed at earlier time points, the 24 h reaction time resulted in a distribution that was no longer represented by a Gaussian distribution, but rather was skewed to the right due to the crystal growth along the radial axis (Figure 3d). The particles varied from long nanorods with L/D of ~15 at 6 h to nanowires with L/D in the range of 60–90 at 16 and 24 h.

When aqueous 5 M NaOH was used to increase the initial pH to 13.70, there was a further reduction in particle diameter (Figure 4a–c), with the majority of particle diameters ranging from 15 to 100 nm. Nanorods produced after 6 h (Figure 4a), underwent crystal growth resulting in the formation of long nanowires by 16 h, the majority of which had diameters of ~25 nm (Figure 4b). Further hydrothermal treatment induced radial crystal growth resulting in a bimodal distribution of diameters, with nanowires having diameters in the ranges of 25 to 50 nm and 55 to 75 nm (Figure 4c$_{ii}$). In contrast to the crystal growth observed at lower pH (5.20 and 7.50), the nonlinear regression curves for pH 13.70 did not display as large an increase in breadth at 24 h (Figure 4d), although there was a slight increase in mean diameter. Particles varied from long nanorods with L/D ~ 17 at 6 h to nanowires with L/D in the range of 60 to 100 at 16 and 24 h. We also assessed whether processing (sedimentation and grinding) affected the morphology of the micro- and nanowires. Using SEM, we found no apparent difference in the morphology of samples that were processed (Figures 2–4) versus those that were not (see Figure S1 in the Supporting Information).

The average particle diameters (Table 1) showed no statistical differences ($p > 0.05$) between powders produced at 6 and 16 h for any of the initial pH values, indicating that any observed growth occurs exclusively at the long axis of the particles. However, prolonging the hydrothermal treatment to 24 h resulted in significant increases ($p < 0.05$) in the nanowire diameter as crystal growth occurred at the radial axes. The effect of initial pH on the particle diameter is not significant ($p > 0.05$) at 6 and 16 h. However, at 24 h, there were significant decreases in diameter with increasing pH ($p < 0.05$).

These results demonstrate the ability to produce nanorods and nanowires with tunable aspect ratios by applying a

dx.doi.org/10.1021/am201735k | ACS Appl. Mater. Interfaces 2012, 4, 1490–1499

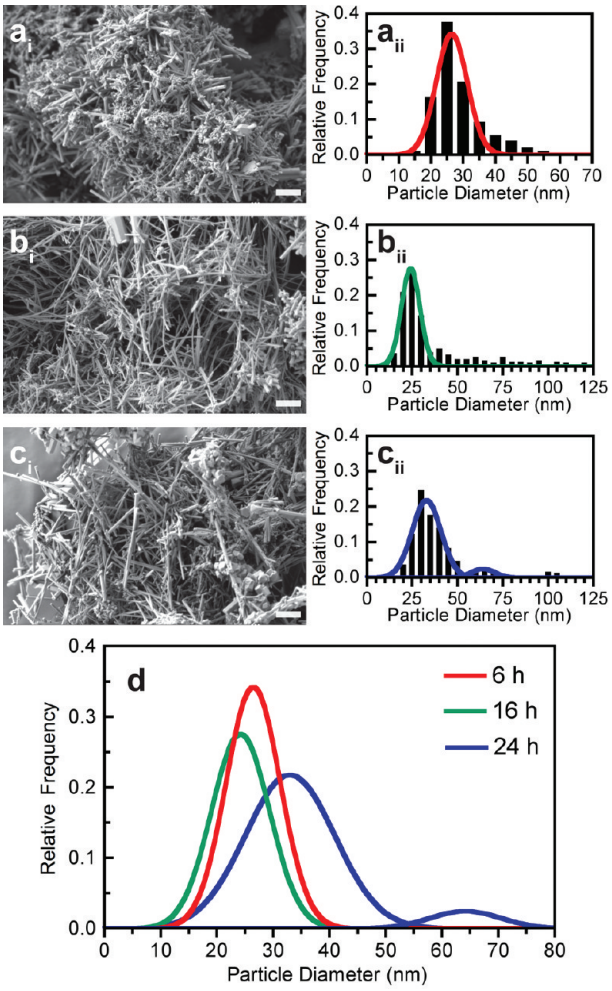

Figure 4. Hydrothermal synthesis at pH 13.70: (i) SEM images and (ii) particle diameter frequency distribution plots of CaP gel powders after hydrothermal treatment for (a) 6, (b) 16, and (c) 24 h. Hydrothermal time effect illustrated by (d) nonlinear regression curves of the particle diameter distributions obtained from measuring 100 particle diameters for three fields of view (n = 300). Scale bar = 500 nm.

Table 1. Particle Diameter of Sol–Gel–Hydrothermal Powders

	particle diameter (nm)[a]		
pH	6 h	16 h	24 h
5.20	32.6 ± 0.5[a]	36.3 ± 0.6[a]	343.2 ± 10.5[b]
7.50	38.9 ± 1.3[a]	38.9 ± 0.6[a]	65.8 ± 2.3[c]
13.70	29.8 ± 0.7[a]	38.3 ± 1.5[a,d]	44.2 ± 2.3[d]

[a]Particle diameter values are mean ± SD calculated from the average of 3 fields of view and 100 measurements per field of view (n = 300). Statistical significance determined by a two-way ANOVA and a Bonferroni post-test. Effect of hydrothermal time and pH on particle diameter was determined, where matching letters indicate groups with no statistical difference (p > 0.05) in particle diameter values as measured using ImageJ software.

hydrothermal treatment to a dried sol–gel product composed of ACP.

XRD Analysis of Nanoparticles Produced by Hydrothermal Treatment. For all durations of hydrothermal treatment, the XRD spectra of powders produced with an initial pH of 5.20 or 7.50 revealed a crystalline and pure HA (Figure 5a, b). All visible peaks in the XRD spectra could be

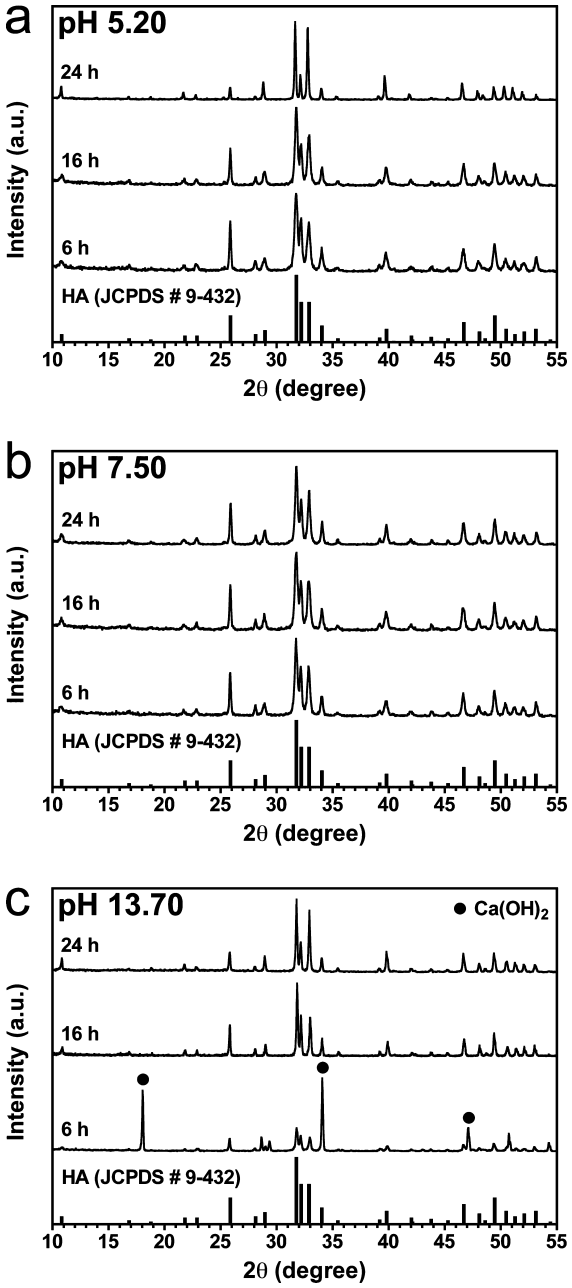

Figure 5. XRD spectra of the CaP gel after hydrothermal treatment in aqueous solvent at initial pH of (a) 5.20, (b) 7.50, and (c) 13.70 for 6, 16, and 24 h. Representative of two independent samples. At the bottom of each spectrum is the Joint Committee on Powder Diffraction Standards (JCPDS # 9–432) pattern for HA.[27]

ascribed to HA, with the major peaks at 2θ = 31.8, 32.2 and 32.9° corresponding to the (211), (112), and (300) diffraction planes of crystalline HA (JCPDS 9–432).[1,27]

XRD spectra of the powders produced at an initial pH of 13.70 (Figure 5c) indicated the presence of $Ca(OH)_2$ in conjunction with HA at 6 h of hydrothermal treatment (revealed by peaks at 2θ = 18.1, 34.5, and 47.2°; JCPDS # 44–1481).[27] However, when the hydrothermal synthesis time was extended to 16 and 24 h, only HA was detected.

The HA powders produced after 24 h, independent of the initial pH, displayed a stronger preference for the (300) XRD reflection (2θ = 32.9°) compared to the JCPDS standard, consistent with crystal growth along the c-axis, which leads to

dx.doi.org/10.1021/am201735k | ACS Appl. Mater. Interfaces 2012, 4, 1490–1499

increased development of the *a*-plane.[12] The XRD spectra of the as produced powders indicated the successful synthesis of crystalline HA nanorods and wires with varying aspect ratios.

FTIR Characterization of Nanoparticles Produced by Hydrothermal Treatment. FTIR analysis confirmed the synthesis of HA after hydrothermal treatment of the CaP gel precursor (Figure 6a–c). Similar bands were observed for

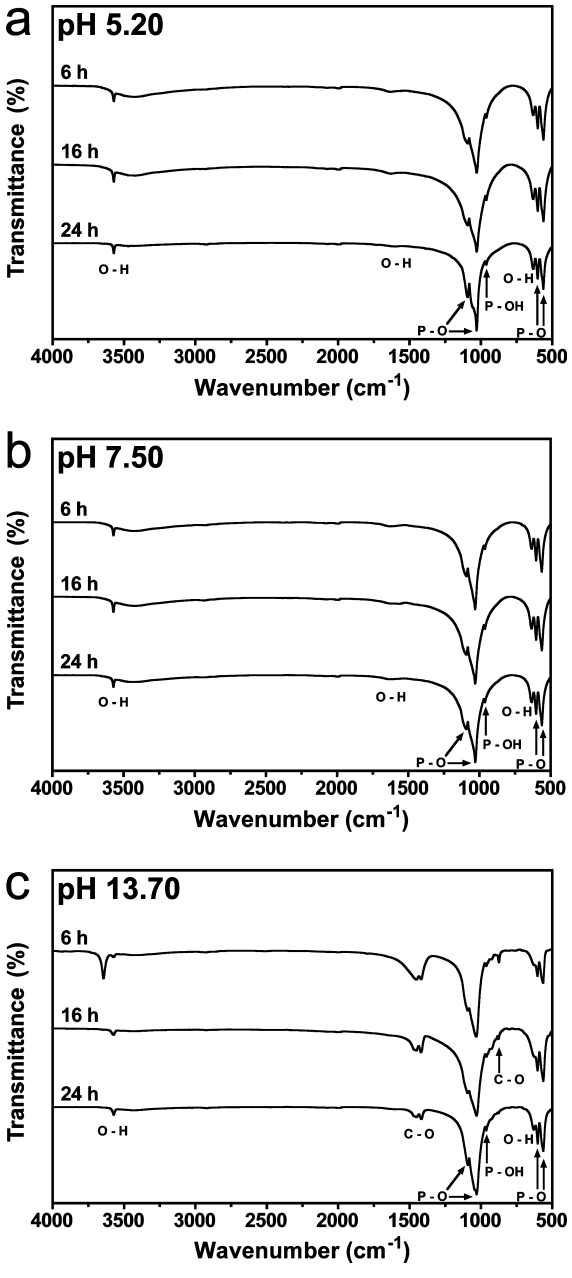

Figure 6. FTIR transmittance spectra of the CaP gel after hydrothermal treatment in aqueous solvent at initial pH of (a) 5.20, (b) 7.50, and (c) 13.70 for 6, 16, and 24 h. Representative of two independent samples.

powders produced at the different initial pH values and spectra are in good agreement with IR data reported for HA.[26] Characteristic peaks of PO_4^{3-} groups are clearly visible at 1091 and 1028 cm^{-1} for the ν_3 asymmetric stretching mode of the P–O bond, and 960 cm^{-1} for the ν_1 symmetric stretching mode of the P–O bond. Additionally, the broad, featureless peak in the range 600–500 cm^{-1}, which was initially seen in the spectra of the CaP gel (Figure 1a), resolved into well-defined bands at 600 and 561 cm^{-1} attributable to the ν_4 bending mode of the O–P–O bond of PO_4^{3-} groups found in apatite.

Hydroxyl (OH) groups were identified by peaks at 3570 and 631 cm^{-1}, ascribed to the stretching and librational modes of hydroxyl anions, the latter indicating a well-developed OH component in the apatite structure.[26,29] CO_3^{2-} substitution in the HA lattice is noticeably absent for HA produced at pH 5.20 and 7.50. CO_3^{2-} substitution was only seen at the elevated pH of 13.70 (Figure 6c), signified by the presence of broad bands at 1450 and 1415 cm^{-1} (A and B-type HA), and sharp peak at 877 cm^{-1} (A-type HA), typical of partial CO_3^{2-} substitution.[1,26] For pH 13.70, the absence of the librational band of OH^- (631 cm^{-1}) at 6 and 16 h suggests possible CO_3^{2-} substitution for OH groups characteristic of A-type HA.[1] The additional stretching peak at 3644 cm^{-1} (Figure 6c) at 6 h is associated with the presence of $Ca(OH)_2$.[30] The decrease in CO_3^{2-} bands at 1450, 1415, and 877 cm^{-1} from 6 to 24 h correlates with the appearance of the OH librational peak at 631 cm^{-1}, consistent with a decrease in CO_3^{2-} substitution. CO_3^{2-} substitution is likely due to the presence of atmospheric CO_2, which dissolved in the H_2O used for slurry preparation and hydrothermal processing.

EDX Elemental Analysis of Nanoparticles Produced by Hydrothermal Treatment. EDX elemental analysis was used to measure the calcium to phosphorus (Ca/P) atomic ratio of HA powders produced after hydrothermal treatment (Table 2), and indicate a predominately stoichiometric HA

Table 2. Ca/P Atomic Ratio of Sol–Gel–Hydrothermal Powders[a]

	Ca/P		
pH	6 h	16 h	24 h
5.20	1.68 ± 0.03[a]	1.60 ± 0.04[a]	1.68 ± 0.04[a]
7.50	1.66 ± 0.06[a]	1.60 ± 0.06[a]	1.71 ± 0.10[a]
13.70	3.71 ± 1.62[b]	1.89 ± 0.03[a]	2.19 ± 0.23[a]

[a]Ca/P values are mean ± SD calculated from the average of 3 fields of view (n = 3). Statistical significance was determined by a two-way ANOVA and a Bonferroni post-test. Effect of hydrothermal time and pH on Ca/P was determined, where matching letters indicate groups with no statistical difference ($p > 0.05$) in Ca/P values as measured using EDX.

crystal (Ca/P ≈ 1.67). There was no significant difference ($p > 0.05$) among the Ca/P ratios of the HA powders synthesized at different pH conditions or hydrothermal treatment times, with the exception of HA produced at pH 13.70 for 6 h ($p < 0.05$). The powder synthesized at pH 13.70 for 6 h is a mixture containing HA and $Ca(OH)_2$, as determined by XRD (Figure 5c), which accounts for the elevated Ca/P atomic ratio. Even at 16 and 24 h, the Ca/P atomic ratio of HA synthesized at pH 13.70 was higher compared to the other pHs (although this was not significant), likely reflecting lower PO_4^{3-} content. FTIR spectra of HA synthesized at pH 13.70 (Figure 6c) indicate the presence of CO_3^{2-} bands for both A and B-type HA. Therefore, it is possible that the higher Ca/P atomic ratios are attributed to partial substitution of CO_3^{2-} for PO_4^{3-} in the HA crystal lattice characteristic of B-type HA.[31]

In summary, the EDX analysis indicated the synthesis of stoichiometric HA at pH 5.20 and 7.50, whereas an initial pH of 13.70 appeared to yield a Ca-rich, B-type CO_3^{2-}-substituted HA. Thus, the EDX results, combined with SEM, XRD, and FTIR, reveal a pH of 13.70 and hydrothermal treatment time of 16–24 h

as ideal for the synthesis of A- and B-type CO_3^{2-}-substituted HA nanowires. In this regard, CO_3^{2-}-substituted HA is thought to be more bioactive than stoichiometric HA.[31]

Characterization of PCL/HA Composites. Composite biomaterials were prepared by combining HA nanowires as reinforcing filler with a PCL matrix. HA nanowires (produced by hydrothermal treatment at pH 13.70 for 24 h) were mixed with PCL in the following ratios (PCL:HA, w/w): 90:10, 80:20, 70:30, 60:40, and 50:50. Fractured surfaces of PCL/HA composites comprising 40 w/w % HA were characterized by SEM and EDX elemental mapping (Figure 7) to determine

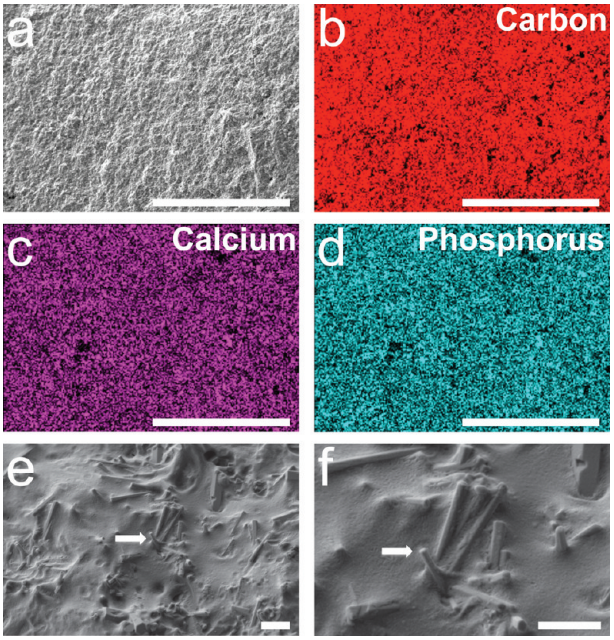

Figure 7. SEM and EDX analysis of PCL/HA composites: (a) SEM image, and EDX elemental mapping of (b) carbon, (c) calcium, and (d) phosphorus of fractured surface of PCL/HA composite (40% HA synthesized by sol–gel-hydrothermal process at pH 13.70 for 24 h) (scale bars = 400 μm). Higher magnification (e, f) SEM images of fractured surface show HA nanowires (e.g., arrow) embedded in the PCL matrix (scale bars = 500 nm).

the distribution of HA nanowires in the PCL matrix. SEM image (Figure 7a) of a fractured PCL/HA composite showed a uniform matrix, free of void spaces. EDX elemental mapping of the same field demonstrates a relatively homogeneous distribution of carbon (Figure 7b), the major elemental component of PCL. Furthermore, EDX mapping of calcium (Figure 7c) and phosphorus (Figure 7d), found exclusively in HA, reveals a uniform distribution. Higher magnification SEM images (Figure 7e, f) clearly showed HA nanowires embedded isotropically within the PCL matrix and in intimate contact with the polymer (arrow). From the SEM analysis and EDX elemental mapping of PCL/HA composite fracture surfaces, we conclude that HA nanowires were uniformly and homogeneously distributed throughout the composite biomaterial.

The Young's modulus and tensile strength of PCL and PCL/HA composites were determined by uniaxial tensile testing (Figure 8). An exponential increase ($p < 0.05$) in the Young's modulus was observed with increase in the HA content (Figure 8a). On the other hand, an increase in HA content resulted in an exponential decrease ($p < 0.05$) in the tensile strength of the composites compared to unfilled PCL (Figure 8b).

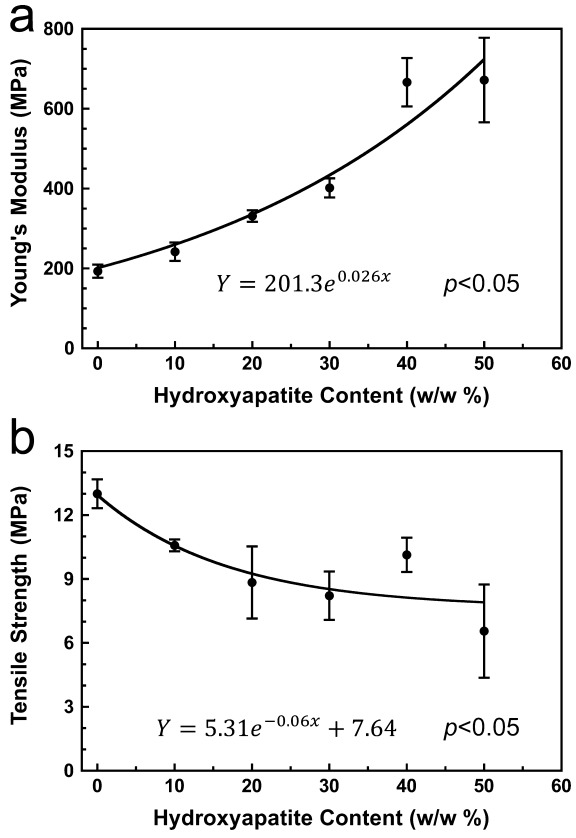

Figure 8. Uniaxial tensile testing of PCL/HA composites: (a) Young's modulus and (b) tensile strength of PCL/HA composites comprising 0–50 w/w % HA synthesized by sol–gel–hydrothermal process at pH 13.70 for 24 h. Young's modulus and tensile strength values are the mean calculated from five independent samples ($n = 5$) measured under uniaxial tension. Error bars are standard deviation. The solid line represents the nonlinear regression analysis fit of tensile test data ($p < 0.05$).

Similarly, compressive modulus and stress at 10% strain increased exponentially ($p < 0.05$) with HA content (Figure 9a, b). It was noted that during compressive testing of PCL and PCL/HA composites, bulging of the cylindrical specimens occurred resulting in an increase in the cross-sectional area of the specimens. This increase in cross-sectional area, and the ductile nature of PCL and PCL/HA composites produced a continuous increase in the measured stress during deformation. Therefore, the compressive stress at 10% strain was chosen to assess the strength of PCL and PCL/HA composites.

There was a significant increase in Young's modulus ($p < 0.05$) after the addition of 20–50% (w/w) HA, with more than a 3-fold increase from 193 MPa for unfilled PCL, to 665 MPa for specimens containing 40–50% (w/w) HA (Table 3). However, a significant decrease in tensile strength ($p < 0.05$) is seen after the addition of 20% (w/w) HA.

Comparable to its effect on Young's modulus, the addition of 20–50% (w/w) HA to PCL significantly increased the compressive modulus ($p < 0.05$) of the composites, with a maximum compressive modulus achieved with 50:50 (w/w) PCL/HA at 487 MPa (Table 2). Furthermore, a significantly greater compressive stress at 10% strain ($p < 0.05$) was observed after the addition of 30–50% (w/w) HA (Table 3). The largest stress value was observed for composites containing 50% (w/w) HA, with a value of 19.9 MPa as compared to 12.7 MPa for unfilled PCL.

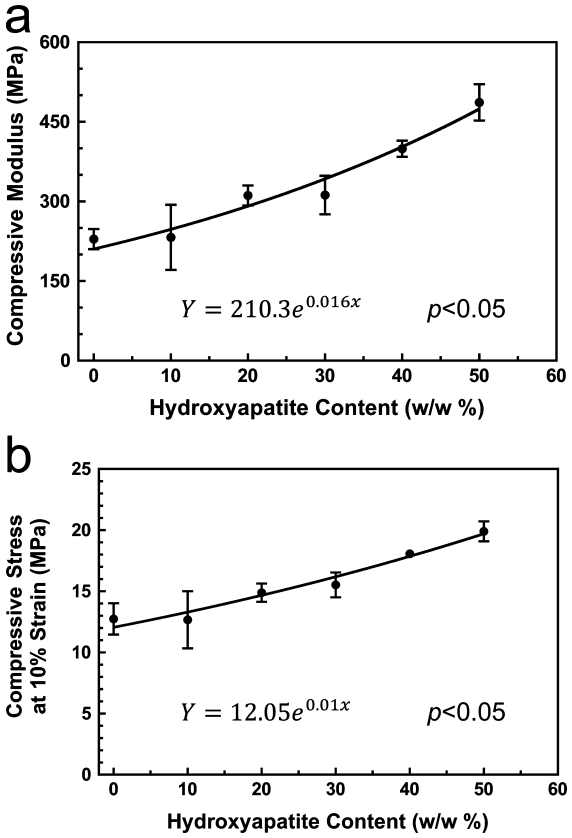

Figure 9. Compressive testing of PCL/HA composites: (a) Compressive modulus and (b) compressive stress at 10% strain of PCL/HA composites comprising 0–50 w/w % HA synthesized by sol–gel-hydrothermal process at pH 13.70 for 24 h. Young's modulus and tensile strength values are the mean calculated from five independent samples (n = 5) measured under compression. Error bars are standard deviation. The solid line represents the nonlinear regression analysis fit of the compressive test data (p < 0.05).

4. DISCUSSION

The synthesis of HA with nanowire morphology has been the subject of extensive research. The sol–gel–hydrothermal process described in the present study provides a novel method for the synthesis of HA with micro- and nanowire morphologies, without the use of organic solvents or surfactants. The synthesis of an amorphous precursor via a sol–gel approach in combination with hydrothermal crystallization results in a high-purity product and provides control over HA particle diameter and length.

The formation of ACP in the sol–gel process occurs via the following stages: 1) hydrolysis of the phosphite sol, 2) interaction with the Ca^{2+} sol to produce colloidal CaP intermediates consisting of Ca–O–P bonds, which are thought to be stabilized by electrostatic repulsive forces and have oligomeric dimensions on the order of a few nanometers (polycondensation),[29] and 3) drying of the sol at 80 °C where ethanol and H_2O are removed, resulting in thermal dehydration and further polycondensation of the colloidal CaP intermediates forming more Ca–O–P bonds and producing a dried CaP gel.[10] FTIR spectra of the CaP gel revealed that the CaP intermediates are amorphous. The spectra also suggested an incomplete reaction between the hydrolyzed phosphite and Ca^{2+} sol during the 24 h aging process. The visible P═O and P–H bands are likely due to the presence of hydrolyzed phosphite precursors in the CaP gel.[29] However the presence of the hydrolyzed phosphite precursor does not seem to disturb the formation of HA during the hydrothermal process.

The 24 h aging step during sol–gel preparation is sufficient to produce a pure apatite-like ACP intermediate as shown in a previous study,[32] and confirmed by FTIR of the CaP gel in the present study. The dried CaP gel is an agglomeration of small particles with dimensions in the nanoscale range (~ 8 nm in diameter).[29] These particles are assembled through weak van der Waals attractive forces, which allow for their facile dispersion and dissolution in aqueous solvents prior to hydrothermal processing.[29] It is this critical feature of the CaP gel precursor that allows for the successful synthesis of HA nanowires by hydrothermal processing.[33]

Typical hydrothermal crystallization involves a transformation process via dissolution and precipitation where amorphous nanoparticles act as a precursor for the formation of small crystalline nuclei (Figure 10a).[23] In the present study, the dissolution of the ACP intermediate in the hydrothermal solution provided a supersaturated medium containing apatite precursors. Subsequently, upon heating of the hydrothermal vessel, the energy input and high-pressure conditions produced crystalline nuclei that grew to form HA nanorods and wires.

The growth of the HA nanowires and the resulting particle morphology is governed by an Ostwald ripening process and diffusion-controlled crystal growth (Figure 10). The Ostwald ripening and Gibbs–Thompson theory state that larger particles grow at the expense of dissolving smaller particles, which are inherently less stable than the larger ones.[34] In diffusion-controlled crystal growth, the concentration of the ACP in the bulk solution is a critical factor.[35]

During crystal growth, the ACP diffuses from the bulk solution and approaches the solution-crystal interface. The autogenous pressure and high energy input of the hydrothermal process accelerates Brownian motion and provides efficient circulation of the ACP.[36] The concentration of ACP at the solution–crystal interface governs the solubility of the HA

Table 3. Mechanical Properties of PCL/HA Composites[a]

PCL:HA (w/w)	Young's modulus (MPa)	tensile strength (MPa)	compressive modulus (MPa)	compressive stress at 10% strain (MPa)
100:0	193.1 ± 14.7[a]	13.0 ± 0.6[a]	229.0 ± 17.0[a]	12.7 ± 1.1[a]
90:10	241.8 ± 20.7[a,b]	10.6 ± 0.2[a,b]	232.3 ± 54.7[a]	12.7 ± 2.1[a]
80:20	331.3 ± 12.8[b,c]	8.8 ± 1.5[b,c]	311.3 ± 17.0[b]	14.9 ± 0.7[a,b]
70:30	401.8 ± 21.5[c]	8.2 ± 1.0[b,c]	312.0 ± 32.5[b]	15.5 ± 0.9[b]
60:40	666.4 ± 54.3[d]	10.1 ± 0.7[b]	399.2 ± 13.6[c]	18.1 ± 0.2[c]
50:50	671.8 ± 94.6[d]	6.6 ± 2.0[c]	486.5 ± 30.5[d]	19.9 ± 0.7[c]

[a]Mechanical properties are mean ± SD calculated from the average of five independent specimens (n = 5) measured under uniaxial tension and compression. Statistical significance determined by a one-way ANOVA and Tukey's multiple comparison test. Effect of HA filler content on mechanical properties of PCL/HA composites were determined, where matching letters indicate groups with no statistical difference (p > 0.05).

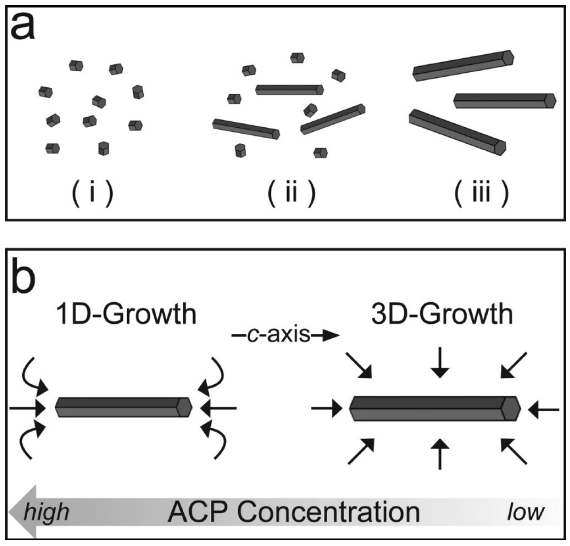

Figure 10. Schematic diagram showing (a) hydrothermal crystallization process involving (i) supersaturation of ACP nanoparticles resulting in the formation of crystalline nuclei, followed by (ii) crystal growth of large nanowires at the cost of smaller, less stable crystals, and (iii) Ostwald ripening process.[23,34] The growth of HA nanowires is a (b) diffusion-controlled crystal growth process, which is governed by the ACP concentration in the bulk resulting in either 1D or 3D growth of HA.[35] Arrows near the crystal indicate the diffusion direction of the ACP molecules.

crystal faces by either rapid growth onto, or dissolution from the different faces depending on the concentration.[35] The atomic structure of the HA unit cell makes the interfacial free energy of the (001) plane (perpendicular to the *c*-axis) greater than the other faces.[37] At a high critical concentration of ACP in the bulk solution, the chemical potential of the ACP is significantly greater than the chemical potential of the (001) face of HA.[35] At this stage, 1D growth occurs as the metastable ACP colloids migrate to the (001) face, causing the crystals to grow exclusively along the *c*-axis of HA. Such growth gives rise to the constant particle diameter and increasing particle length seen at early hydrothermal times from 6 to 16 h in Figures 2–4. When the hydrothermal process is extended to 24 h, the concentration of the ACP drops to a level where the overall chemical potential of the bulk solution decreases. This makes it difficult for the diffusion flux of ACP to preferentially go to the (001) face of HA. The result is 3D growth, in which ACP is shared by each face of the HA particles and both particle diameter and length increase, giving rise to the broad distribution of particle diameters seen at pH 5.20, the skewed distribution at pH 7.50, and the bimodal distribution at pH 13.70.

As evident from the XRD spectra, the evolution of the HA from 6 to 24 h at each pH value was associated with a relative increase in the (300) reflection. This in turn signifies expansion of the *a*-plane of HA, which corresponds to crystal growth along the *c*-axis.

A marked effect of pH on particle diameter was observed. The solubility of HA decreases with increase in pH.[1] As a result of the lower solubility, smaller HA particles precipitate out of solution at higher pH levels as indicated by the significantly lower particle diameter values at 24 h.

During in vivo and in vitro applications of biomaterials, maintaining the porosity and preventing collapse of the porous structure of scaffolds is a determining factor in their success.[4] In PCL/HA composites, the HA nanowires were uniformly distributed throughout the PCL matrix and mechanical testing demonstrated the reinforcing ability of HA nanowires. Nanoscale HA crystals impart the stiffness and strength of bioceramics to the toughness and ductility of PCL. When HA nanoparticles are used as filler materials in polymer matrices, the nanoparticle diameter and aspect ratio govern the strengthening effect. The ideal filler material has the smallest possible particle diameter, while maximizing the particle length and thereby having a large aspect ratio.[6,38] HA nanowires synthesized at pH 13.70 for 24 h were selected as the filler for reinforcement of PCL composites because the longest observable particle lengths were seen at 24 h and the smallest particle diameters were obtained at pH 13.70. Both the Young's and compressive moduli of PCL/HA composites were significantly greater as compared to unfilled PCL. This increase in stiffness of the composite material will be beneficial for bone tissue engineering scaffolds. Furthermore, the inclusion of nanoscale HA particles will impart the superior bioactive and osteoconductive properties of HA to the composite materials.[3,16]

5. CONCLUSION

The novel sol–gel–hydrothermal process described above is an effective method for the synthesis of phase-pure HA. The combination of a nanoscale ACP precursor produced by sol–gel chemistry, with a hydrothermal crystallization process results in the formation of HA with micro- and nanowire morphologies. This surfactant- and solvent-free process allows for tunable particle morphology, while maintaining the purity of the final HA product. These HA nanowires are effective fillers for the reinforcement of PCL/HA composites.

■ ASSOCIATED CONTENT

Ⓢ Supporting Information

Supporting Figure S1 shows SEM images of HA synthesized under selected hydrothermal conditions (pH 5.20, 7.50, and 13.70 for 24 h) to evaluate the morphology of micro- and nanowires as synthesized prior to processing (sedimentation and grinding). This material is available free of charge via the Internet at http://pubs.acs.org/.

■ AUTHOR INFORMATION

Corresponding Author

*E-mail: arizkalla@eng.uwo.ca.

Notes

The authors declare no competing financial interest.

■ ACKNOWLEDGMENTS

These studies were funded by the Natural Sciences and Engineering Research Council of Canada (NSERC) and the Canadian Institutes of Health Research (CIHR). D. O. Costa was supported in part by the Joint Motion Program – A CIHR Training Program in Musculoskeletal Health Research and Leadership. SEM micrographs and EDX analysis were performed by Dr. Todd Simpson and Tim Goldhawk of the Western Nanofabrication Facility. Poly(ε-caprolactone) was generously donated by Solvay Chemicals Inc. We thank Bedilu Allo for valuable advice and stimulating discussion.

■ REFERENCES

(1) LeGeros, R. Z. *Monogr. Oral Sci.* **1991**, *15*, 1–201.
(2) Hott, M.; Noel, B.; Bernache-Assolant, D.; Rey, C.; Marie, P. J. *J. Biomed. Mater. Res.* **1997**, *37* (4), 508–516.

(3) Okuda, T.; Ioku, K.; Yonezawa, I.; Minagi, H.; Gonda, Y.; Kawachi, G.; Kamitakahara, M.; Shibata, Y.; Murayama, H.; Kurosawa, H.; Ikeda, T. *Biomaterials* **2008**, *29* (18), 2719−2728.
(4) Lickorish, D.; Guan, L.; Davies, J. E. *Biomaterials* **2007**, *28* (8), 1495−1502.
(5) Roeder, R. K.; Sproul, M. M.; Turner, C. H. *J. Biomed. Mater. Res., A* **2003**, *67* (3), 801−812.
(6) Wei, G.; Ma, P. X. *Biomaterials* **2004**, *25* (19), 4749−4757.
(7) Muller, F.; Gbureck, U.; Kasuga, T.; Mizutani, Y.; Barralet, J. E.; Lohbauer, U. *J. Am. Ceram. Soc.* **2007**, *90* (11), 3694−3697.
(8) Neira, I. S.; Kolen'ko, Y. V.; Kommareddy, K. P.; Manjubala, I.; Yoshimura, M.; Guitian, F. *ACS Appl. Mater. Interfaces* **2010**, *2* (11), 3276−3284.
(9) Eshtiagh-Hosseini, H.; Housaindokht, M. R.; Chahkandi, M. *Mater. Chem. Phys.* **2007**, *106* (2−3), 310−316.
(10) Liu, D. M.; Troczynski, T.; Tseng, W. J. *Biomaterials* **2001**, *22* (13), 1721−1730.
(11) Fathi, M. H.; Hanifi, A. *Mater. Lett.* **2007**, *61* (18), 3978−3983.
(12) Neira, I. S.; Kolen'ko, Y. V.; Lebedev, O. I.; Van Tendeloo, G.; Gupta, H. S.; Guitian, F.; Yoshimura, M. *Cryst. Growth Des.* **2009**, *9* (1), 466−474.
(13) Mizutani, Y.; Hattori, M.; Okuyama, M.; Kasuga, T.; Nogami, M. *J. Eur. Ceram. Soc.* **2005**, *25* (13), 3181−3185.
(14) Zhang, H.; Darvell, B. W. *Acta Biomater.* **2010**, *6* (8), 3216−3222.
(15) Zhou, H.; Lee, J. *Acta Biomater.* **2011**, *7* (7), 2769−2781.
(16) Sun, F.; Zhou, H.; Lee, J. *Acta Biomater.* **2011**, *7* (11), 3813−3828.
(17) Chung, E. J.; Qiu, H.; Kodali, P.; Yang, S.; Sprague, S. M.; Hwong, J.; Koh, J.; Ameer, G. A. *J. Biomed. Mater. Res., A* **2011**, *96* (1), 29−37.
(18) Lin, K. L.; Liu, X. G.; Chang, J.; Zhu, Y. J. *Nanoscale* **2011**, *3* (8), 3052−3055.
(19) Lin, K. L.; Chang, J.; Liu, X. G.; Chen, L.; Zhou, Y. L. *Crystengcomm* **2011**, *13* (15), 4850−4855.
(20) Cao, M. H.; Wang, Y. H.; Guo, C. X.; Qi, Y. J.; Hu, C. W. *Langmuir* **2004**, *20* (11), 4784−4786.
(21) Wei, K.; Lai, C.; Wang, Y. J. *J. Macromol. Sci., Pure Appl. Chem.* **2006**, *43* (10), 1531−1540.
(22) Sun, Y. X.; Guo, G. S.; Tao, D. L.; Wang, Z. H. *J. Phys. Chem. Solids* **2006**, *68* (3), 373−377.
(23) Chen, J. D.; Wang, Y. J.; Wei, K.; Zhang, S. H.; Shi, X. T. *Biomaterials* **2007**, *28* (14), 2275−2280.
(24) Zhang, C. M.; Yang, J.; Quan, Z. W.; Yang, P. P.; Li, C. X.; Hou, Z. Y.; Lin, J. *Cryst. Growth Des.* **2009**, *9* (6), 2725−2733.
(25) Cullity, B. D., *Elements of X-ray diffraction*; Addison-Wesley: Reading, MA, 1967; p 514.
(26) Koutsopoulos, S. *J. Biomed. Mater. Res.* **2002**, *62* (4), 600−612.
(27) Joint Committee on Chemical Analysis by Powder Diffraction Methods. *Powder Diffraction File*, revised ed.; American Society for Testing and Materials: Philadelphia, PA, 1960.
(28) Chou, Y. F.; Chiou, W. A.; Xu, Y. H.; Dunn, J. C. Y.; Wu, B. M. *Biomaterials* **2004**, *25* (22), 5323−5331.
(29) Liu, D. M.; Yang, Q.; Troczynski, T.; Tseng, W. J. *Biomaterials* **2002**, *23* (7), 1679−1687.
(30) Kalinkin, A. M.; Kalinkina, E. V.; Zalkind, O. A.; Makarova, T. I. *Inorg. Mater.* **2005**, *41* (10), 1073−1079.
(31) Gibson, I. R.; Bonfield, W. *J. Biomed. Mater. Res.* **2002**, *59* (4), 697−708.
(32) Liu, D. M.; Troczynski, T.; Tseng, W. J. *Biomaterials* **2002**, *23* (4), 1227−1236.
(33) Hou, Y. D.; Hou, L.; Zhang, T. T.; Zhu, M. K.; Wang, H.; Yan, H. *J. Am. Ceram. Soc.* **2007**, *90* (6), 1738−1743.
(34) Lalena, J. N., *Inorganic Materials Synthesis and Fabrication*; Wiley-Interscience: Hoboken, NJ, 2008; Vol. *iii*, p 303.
(35) Peng, X. G.; Peng, Z. A. *J. Am. Chem. Soc.* **2001**, *123* (7), 1389−1395.
(36) Yu, S. H.; Liu, B.; Mo, M. S.; Huang, J. H.; Liu, X. M.; Qian, Y. T. *Adv. Funct. Mater.* **2003**, *13* (8), 639−647.
(37) Kim, T. G.; Park, B. *Inorg. Chem.* **2005**, *44* (26), 9895−9901.
(38) Liu, T. Y.; Chen, S. Y.; Liu, D. M. *J. Biomed. Mater. Res., B: Appl. Biomater.* **2004**, *71B* (1), 116−122.